

## RESEARCH ARTICLE

10.1029/2017JA024199

## Key Points:

- Daytime/nighttime occurrences of ionospheric irregularities at a local scale for the first time were revealed by combining RO and GB GPS data
- *E* region irregularities were prominent in summer showing differences between RO and GB observations
- A sign of coupling of *E* and *F* regions during nighttime has been likely indicated by simultaneous observations from RO profile data

## Correspondence to:

 Z. Liu,  
 lszzliu@polyu.edu.hk

## Citation:

Yang, Z., & Liu, Z. (2018). Low-latitude ionospheric density irregularities and associated scintillations investigated by combining COSMIC RO and ground-based Global Positioning System observations over a solar active period. *Journal of Geophysical Research: Space Physics*, 123, 3998–4014. <https://doi.org/10.1029/2017JA024199>

Received 28 MAR 2017

Accepted 10 APR 2018

Accepted article online 19 APR 2018

Published online 2 MAY 2018

## Low-Latitude Ionospheric Density Irregularities and Associated Scintillations Investigated by Combining COSMIC RO and Ground-Based Global Positioning System Observations Over a Solar Active Period

 Zhe Yang<sup>1</sup>  and Zhizhao Liu<sup>1</sup> 
<sup>1</sup>Department of Land Surveying and Geo-Informatics, The Hong Kong Polytechnic University, Hong Kong

**Abstract** This study for the first time presents a locally integrated analysis of occurrences of ionospheric *E* and *F* region irregularities/scintillations in southeast China, by employing radio occultation (RO) profile data retrieved from Constellation Observing System for Meteorology, Ionosphere, and Climate (COSMIC) satellites and observations from a ground-based Global Navigation Satellite System receiver over a solar active period from 2014 to 2015. Their occurrences in both nighttime and daytime were examined by using both amplitude scintillation index ( $S_4$ ) and the rate of change of total electron content index. It is found that (1) *F* region irregularities occurred predominantly during 20–03 local time (LT) and exhibited maximum (minimum) during equinoxes (solstices) and equinoctial (solstice) asymmetry. Their geographic mapping reveals the maximum occurrence in the westward tilted structure of equatorial plasma bubbles. In addition, the altitude-time variations indicate that their occurrences at higher altitudes were prevailing at 20–22 LT. (2) The *E* region irregularities were found prominently during 15–00 LT at altitudes of 90–110 km with an even geographic distribution. Their occurrences with maximum in summer (May–August) were distinctly detected by RO observations but insignificantly by ground-based observations. (3) By examining simultaneous observations of *E* and *F* region irregularities, it is found that they appeared absent during 21–00 LT and predominant after midnight. This could be related to the weakening/disruption of sporadic *E* ( $E_s$ ) layers during the development of equatorial plasma bubbles. A sign of coupling of *E* and *F* regions during nighttime is likely revealed from RO profile data.

### 1. Introduction

Ionospheric irregularities caused by abnormal variations in plasma or electron densities have been extensively investigated, both experimentally and theoretically (e.g., Arras et al., 2008; Fejer & Kelley, 1980; Kil & Heelis, 1998, and references therein). The physical processes involved in the generation of ionospheric irregularities are complex and still not fully understood (e.g., Abdu, 2001; Basu et al., 2009, and references therein). Given rise to random fluctuations in the amplitude and phase of transionospheric radio signals, known as ionospheric scintillations, ionospheric plasma irregularities have become a major concern for satellite communication systems (e.g., Kintner et al., 2007). Therefore, research into ionospheric irregularities has both scientific and practical values.

Sporadic *E* plasma irregularities (also called  $E_s$  layers), appear sporadically in an altitude range of 90–120 km, are layered structures of enhanced electron density in the *E* region of the ionosphere. It is generally accepted that the  $E_s$  layers are formed because of the convergence of metallic ion flux induced by neutral wind shear (e.g., Chu et al., 2014). Some also suggested that the combination of wind shear theory and meteor ionization mechanism explains the formation of  $E_s$  layers more completely (Yeh et al., 2014). The occurrence of  $E_s$  layers depends on local time, season, altitude, and geographic location (Arras et al., 2008; Chu et al., 2014; Wu et al., 2005). In addition to  $E_s$  layers, equatorial plasma bubbles (EPBs) are ionospheric plasma irregularities that occur in the equatorial *F* region. They are large regions of depleted ionospheric plasma density formed at the bottom of the *F* region in the postsunset period (Woodman & La Hoz, 1976). The presence of EPBs is widely believed to be caused by the generalized Rayleigh-Taylor (R-T) instability that forms at the bottom of the *F* region under favorable conditions (Schunk & Nagy, 2009, and references therein). Multiple factors play a role in the generation of EPBs by initiating the growth of R-T instability, including the vertical drift of the *F* layer, meridional wind, field line-integrated conductivity, and perturbation sources (Abdu, 2001; Basu et al., 1996; Singh et al., 1997). So far,

describing the variability of EPBs on a day-to-day basis remains a significant challenge (e.g., Basu et al., 2009; Carter et al., 2014).

Many efforts have put into searching the source mechanism responsible for the day-to-day variability of EPBs (e.g., Mendillo et al., 2001; Tsunoda, 2005, 2006, 2010). Based on observational investigations, it has been suggested that low-latitude *Es* variability plays an important role on the day-to-day variability of EPBs via the growth rate of the R-T instability. The *Es* layer instability can act as a seed of EPBs by modulating the plasma in the form of large-scale wave structure (e.g., Tsunoda, 2007), and the postsunset *Es* layers are capable of influencing the formation of EPBs by changes in the field line-integrated Pedersen conductivity of *Es* layers (Joshi et al., 2013). Additionally, it has been indicated that the electrodynamic processes involving in the development of EPBs may in turn control the formation of *Es* layers (e.g., Abdu et al., 2003; Patra et al., 2005) as well as valley region irregularities (occurring at altitudes of 130–180 km during nighttime; e.g., Yokoyama et al., 2005). The geneses of EPBs and *Es* are thus interrelated as resulting from the coupling of the ionospheric *E* and *F* region dynamos.

In the present study, we investigate the concurrent occurrences of *E* and *F* region irregularities in the southeast China over a solar active period. The investigated area is a typical low-latitude region where ionospheric irregularities occur involving complex electrodynamic processes. Previously, an investigation into the role of postsunset EPBs occurrences that plays in the occurrence of *Es* and valley region irregularities has been conducted (Li, Ning, Patra, et al., 2011), in addition to those into the generation and evolution of EPBs (e.g., Ji et al., 2015; Sun et al., 2016) and the seeding sources for their formation (e.g., Kumar et al., 2017; Yang & Liu, 2016). In this analysis, we analyze the occurrences of *E* and *F* region irregularities for both nighttime and daytime and discuss the linkage between their occurrences by examining simultaneous observations of *E* and *F* region irregularities. The analysis is demonstrated by integrating radio occultation (RO) measurements from Constellation Observing System for Meteorology, Ionosphere, and Climate (COSMIC) satellites and observations from ground-based (GB) Global Positioning System (GPS)/Global Navigation Satellite System receivers.

COSMIC RO measurements can observe ionospheric irregularity distributions covering altitude range from the Earth's surface to 840 km. The COSMIC RO observations have been used to study 3-D global morphologies of scintillations (e.g., Brahmanandam et al., 2012; Liu et al., 2016), morphologies of *Es* layers (e.g., Chu et al., 2014), and equatorial *F* region irregularities (e.g., Carter et al., 2013; Ko & Yeh, 2010). Contrary to those studies mainly focusing on global scale, this study for the first time focuses on a locally integrated analysis of *E* and *F* region irregularities using COSMIC RO data. In the past studies, the data at a single tangent point (TP) are used (Brahmanandam et al., 2012; Carter et al., 2013; Ko & Yeh, 2010; Liu et al., 2016). In our study the profile data of RO events are utilized. This allows us to fully utilize the RO observations in a local region and to examine simultaneous observations in both *E* and *F* regions. We also exploit the RO GPS phase data to derive the rate of change of total electron content index (ROTI, in TECu/s; 1 TECu refers to  $10^{16}$  el/m<sup>2</sup> and GPS L1 signal range of 0.16 m) to study the ionospheric irregularities, in addition to the traditional scintillation indices. Through this analysis, we also discuss the differences between RO and GB GPS data in describing ionospheric irregularities.

The remainder of the paper is organized as follows. First, the data and analysis details are introduced. Then, the general morphology of *E* and *F* region irregularities as observed from the COSMIC RO and GB GPS data is illustrated followed by a detailed analysis of their occurrences for different time of day. Thereafter, a discussion is given based on the observational results. Finally, conclusions are drawn.

## 2. Data and Analysis Details

### 2.1. Data Description

The COSMIC RO GPS data obtained in the altitude range of 70–840 km on a solar active period from 2014 to 2015 are analyzed. The amplitude scintillation index  $S_4$  derived from 50-Hz signal-to-noise intensity over 1 s is used to characterize ionospheric irregularities. This index data, archived at the COSMIC Data Analysis and Archive Center, include both “global” and “profile” parameters. In our analysis, the profile data were used. Only scintillations with  $S_4 \geq 0.2$  during an occultation period are considered, but those with  $S_4 > 2.0$  were considered as outliers and removed. The geolocation of RO observations is assigned to the TP of the line of sight from GPS to COSMIC satellites. The TP's geolocation information was estimated using the positions of the GPS and COSMIC satellites in our study.

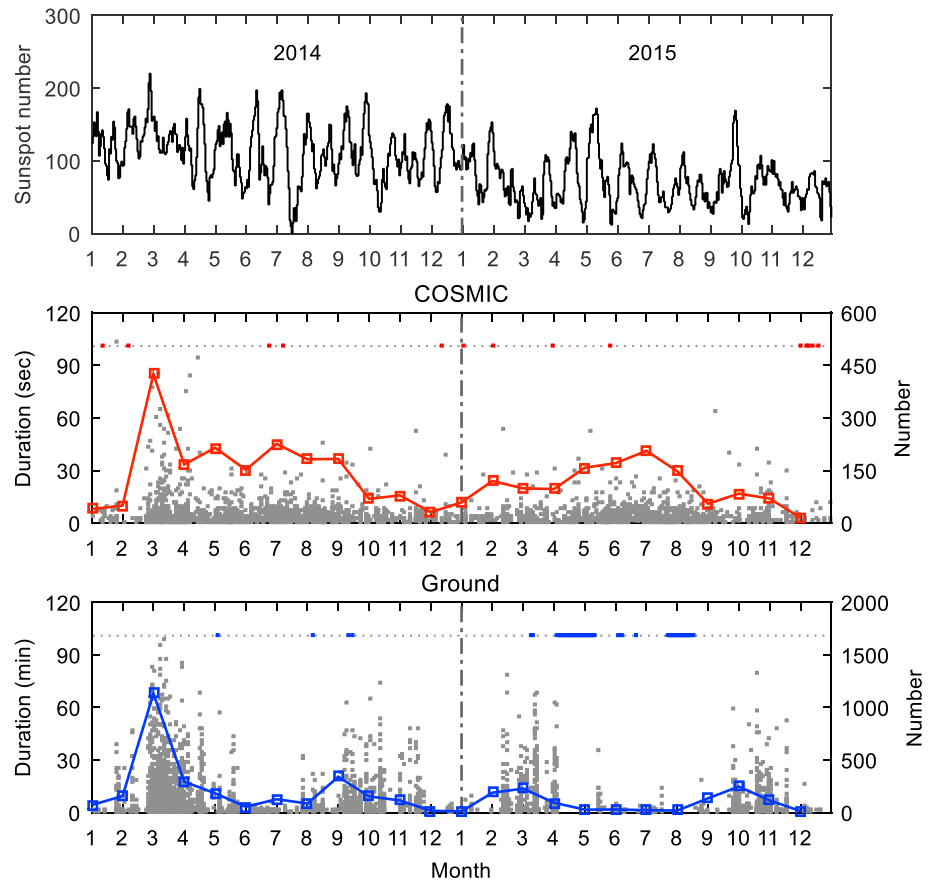


**Figure 1.** Daily total sunspot number (top panel). The duration of scintillations (gray points) and the number of daily scintillation events ( $S_4 \geq 0.2$ ) for Constellation Observing System for Meteorology, Ionosphere, and Climate (COSMIC) radio occultation (middle panel) and ground-based Global Positioning System (bottom panel) during 2014–2015. The period with data outages is marked as red points (radio occultation) and blue points (ground) along the dashed lines.

The GB GPS data were obtained from a Septentrio PolaRxS Pro Global Navigation Satellite System receiver installed at the Hok Tsui station (geographic: 22°12'N, 114°15'E; geomagnetic: 12°23'N, 173°34'W) in the south of Hong Kong. Based on the 100-Hz data output from this receiver, the  $S_4$  index was calculated over 60 s using a 1-s window by the GPS L1 signal for studying ionospheric irregularities. Only scintillations with  $S_4$  values greater than 0.2 and lasting for at least 60 s were considered in the analysis. To reduce multipath effects, only satellite data with elevations greater than 30° were considered. The geolocations of GB observations are represented by the ionospheric pierce point (IPP) in the ionospheric layer.

## 2.2. Analysis Details

This analysis focuses on the region of 17°N–27°N and 109°E–119°E in the southeast China and on a solar active period from 2014 to 2015. Over the study period, a total of 3,770 RO events was observed in the study region, with a daily occurrence of up to 15 RO events. Figure 1 shows the scintillation occurrences and durations of RO and GB GPS signals over the solar active period. In the middle and bottom panels of Figure 1, the periods with RO and GB data outages are indicated by red and blue points, respectively. As shown, the data gaps mainly occurred in April, May, July, and August of 2015 for GB observations. In total, 70 days in 2015 had data outages at the GB station. For the RO data sets, 5 days in 2014 and 8 days in 2015 had data outages.

Detected by both RO and GB observations, the occurrence of scintillations decreased from 2014 to 2015 with the corresponding decline in solar activity, as shown in Figure 1. The durations of RO scintillations had very short durations, typically less than 30 s. The longest of the RO scintillations in 2014 and 2015 lasted for about 100 and 60 s, respectively. However, GB scintillation events lasted for up to 100 and 80 min in 2014

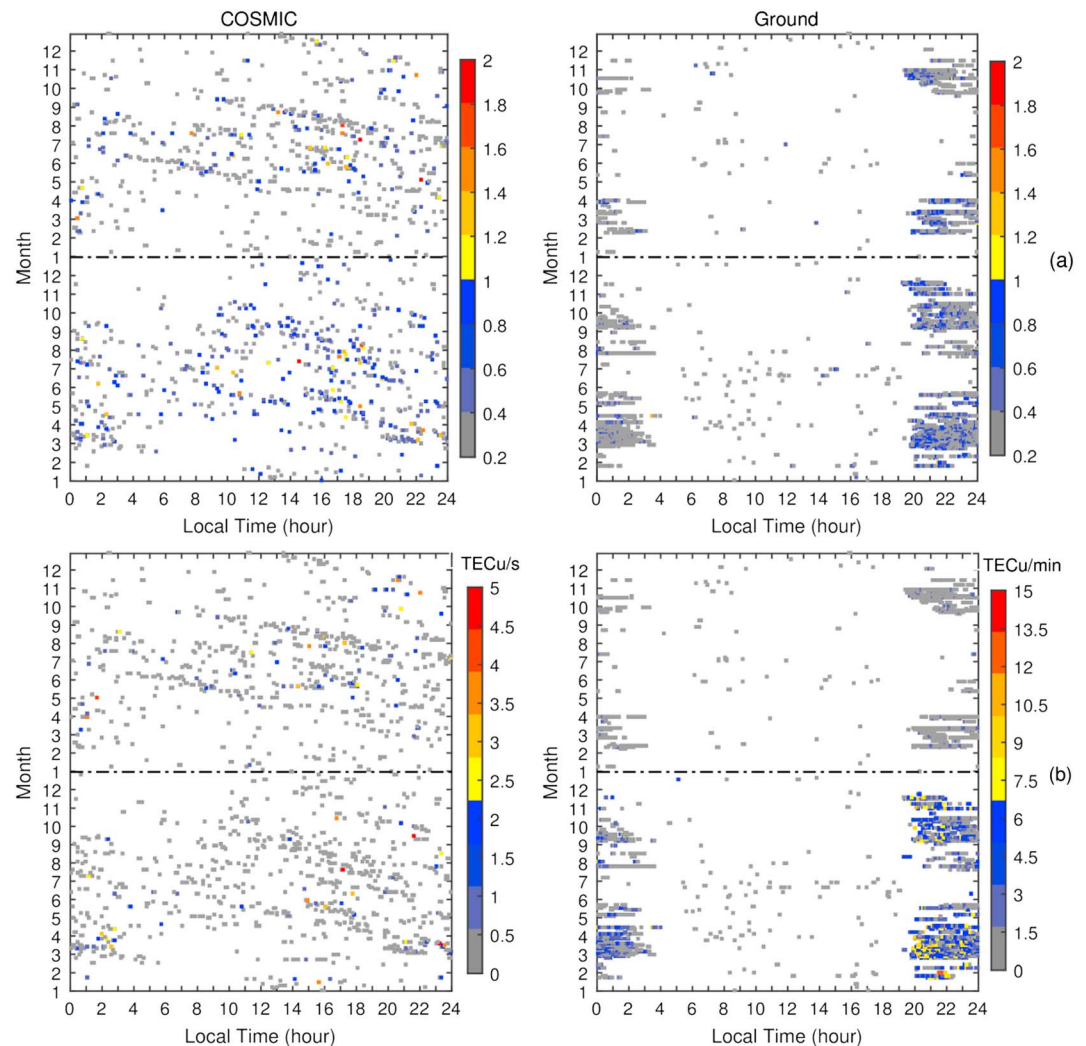


**Figure 2.** Local time-month variations in (a) scintillation amplitudes ( $S_4 \geq 0.2$ ) and (b) rate of change of total electron content index observed by the Constellation Observing System for Meteorology, Ionosphere, and Climate (COSMIC) satellites (left) and the Hok Tsui ground station (right) from 1 January 2014 to 31 December 2015. The black dash-dotted horizontal line in each panel separates the data of 2014 (below) and 2015 (above). The data outages in 2015 were depicted in Figure 1.

and 2015, respectively. The durations of most GB scintillations were less than 30 min. In both sets of GPS observations, the most intense scintillations were observed in March 2014.

In the analysis, in addition to scintillation observations, GPS phase measurements from the COSMIC RO and GB station are utilized for studying ionospheric irregularities. Based on the 1-s dual-frequency GPS phase measurements, ROTI proposed by Pi et al. (1997) is derived to characterize the ionospheric density irregularities during scintillation occurrences. The ROTI is calculated at a 1-s rate over 5 min for the GB observations and over 5 s for the COSMIC RO observations. The 5-s window is chosen because of the short duration of RO events. The following analysis will demonstrate that the COSMIC RO-retrieved ROTI can be an effective index for monitoring the occurrence of ionospheric irregularities.

### 3. Observational Results

#### 3.1. General Morphology of Ionospheric Irregularities

The ionospheric irregularities detected by the COSMIC RO and GB GPS observations are first illustrated in terms of their temporal and spatial variabilities. Figure 2 depicts the local time (LT)-month variations in the

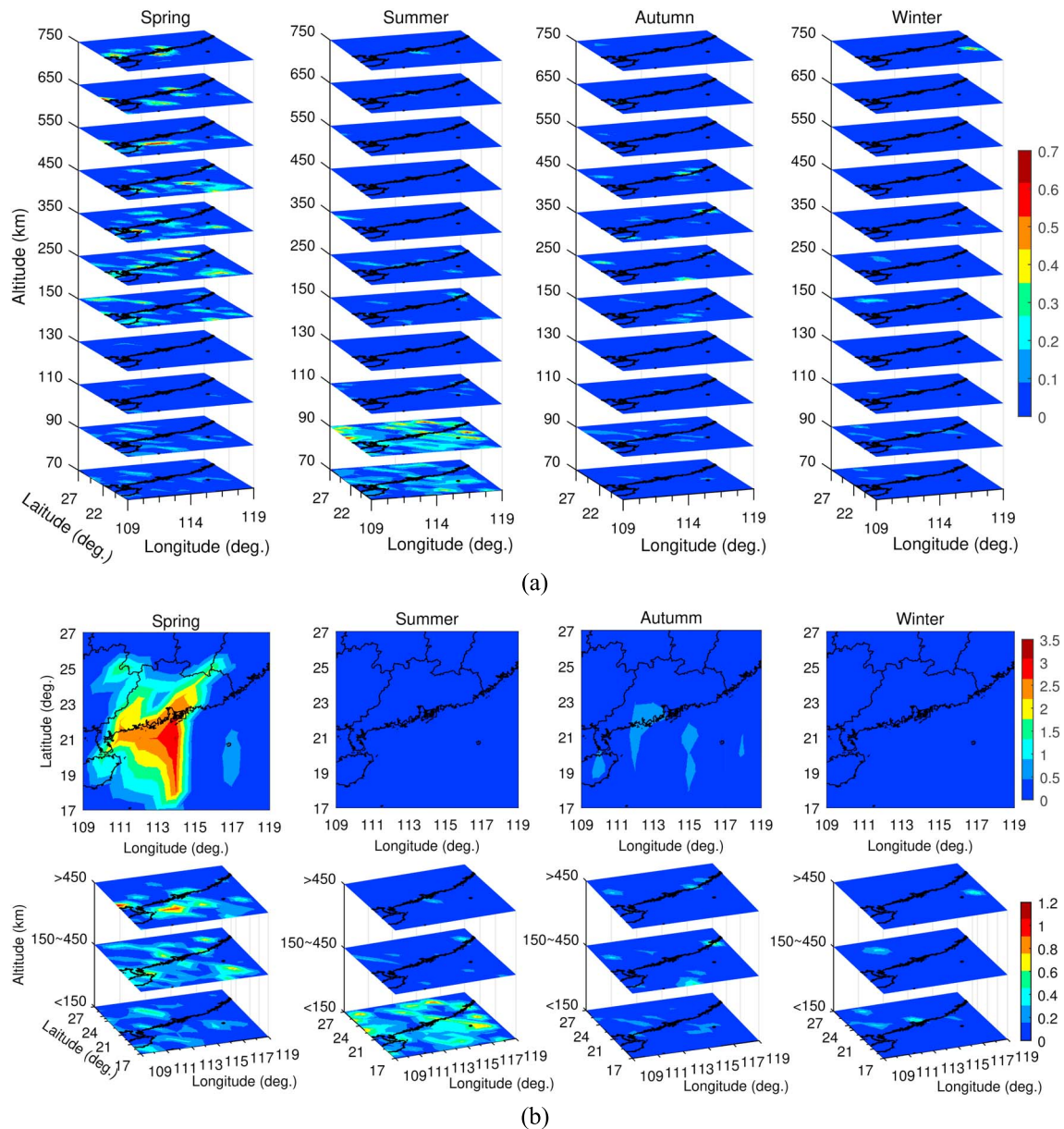


**Figure 3.** The 3-D geographic mapping of ionospheric irregularities for different seasons in 2014: (a) Constellation Observing System for Meteorology, Ionosphere, and Climate data; (b) integrative results of ground-based observation (top) and Constellation Observing System for Meteorology, Ionosphere, and Climate observations (bottom). The ground-based observations were mapped to ionospheric pierce points at an altitude of 350 km. The RO observations were mapped according to their TP information. The occurrence rate (%) was calculated based on the number of scintillations in each  $1^\circ \times 1^\circ$  grid relative to the total number of scintillations in the study region.

ROTI and  $S_4$  values during 2014–2015. One noticeable feature can be seen is that the daily variability of ionospheric irregularities shows differences between the RO and GB observations. As illustrated by the ROTI and  $S_4$  variations, the ionospheric irregularities were detected by the RO observations throughout the day, while by the GB observation they were predominantly seen at nighttime from 20 LT to 03 LT and very few daytime ionospheric irregularities were observed. The nighttime GB scintillations mainly occurred in equinox months (March, April, September, and October), while the daytime GB scintillations appeared prominent in the summer months (May to August).

During the period of 20–03 LT, as seen in Figure 2, the GB ROTI values decrease gradually from above 1.5 TECu/min to below 1.5 TECu/min. This corresponds well with the evolution of EPBs starting at 20 LT

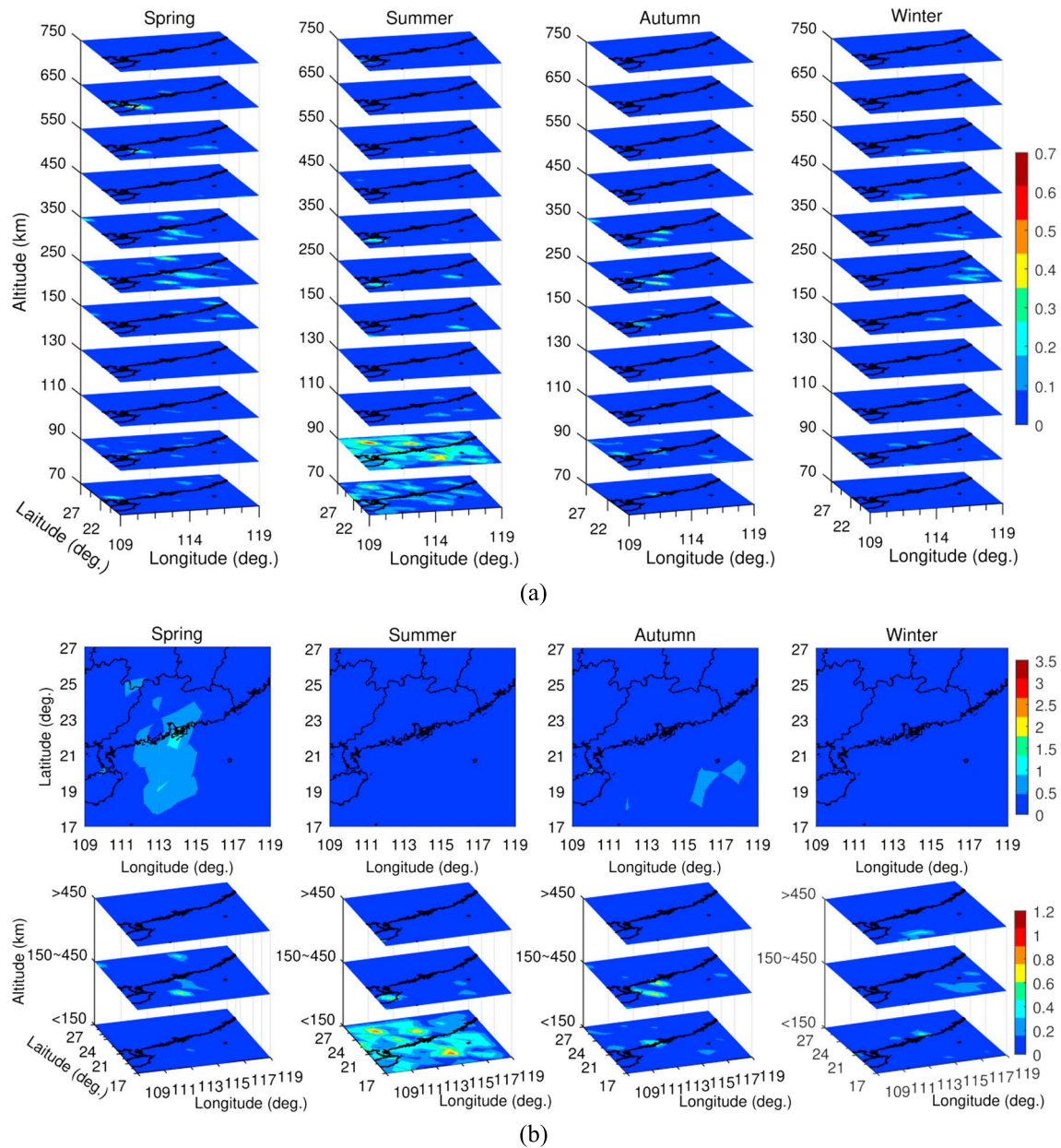


**Figure 4.** Same as Figure 3 but for 2015. The ground-based data outages that occurred in spring and summer (April, May, July, and August) of 2015 were depicted in Figure 1.

with a drift velocity of around 200 m/s and ending after 24 LT with a velocity of more than 50 m/s (Ji et al., 2015). The RO-derived ROTI values do not exhibit the same variations as the GB values because of the short durations of the RO observations. The two sets of GPS observations suggest differences in ionospheric density fluctuations characterized by the 1-s ROTI. In general, the ROTI values associated with RO scintillations are in the range of 0–5 TECu/s, while the GB ROTI values are in the range of 0–15 TECu/min. In comparison, the RO ROTI values are larger. This should be caused by the different time windows in ROTI estimations and the high-speed movement of GPS receivers onboard the COSMIC satellites (Yang & Liu, 2016).

Figures 3 and 4 illustrate the geographic mapping of ionospheric irregularities at different ionospheric layers during four seasons of 2014 and 2015, respectively. The ionospheric irregularities were examined based on the RO and GB scintillation data. As shown, the occurrences of ionospheric irregularities differ at

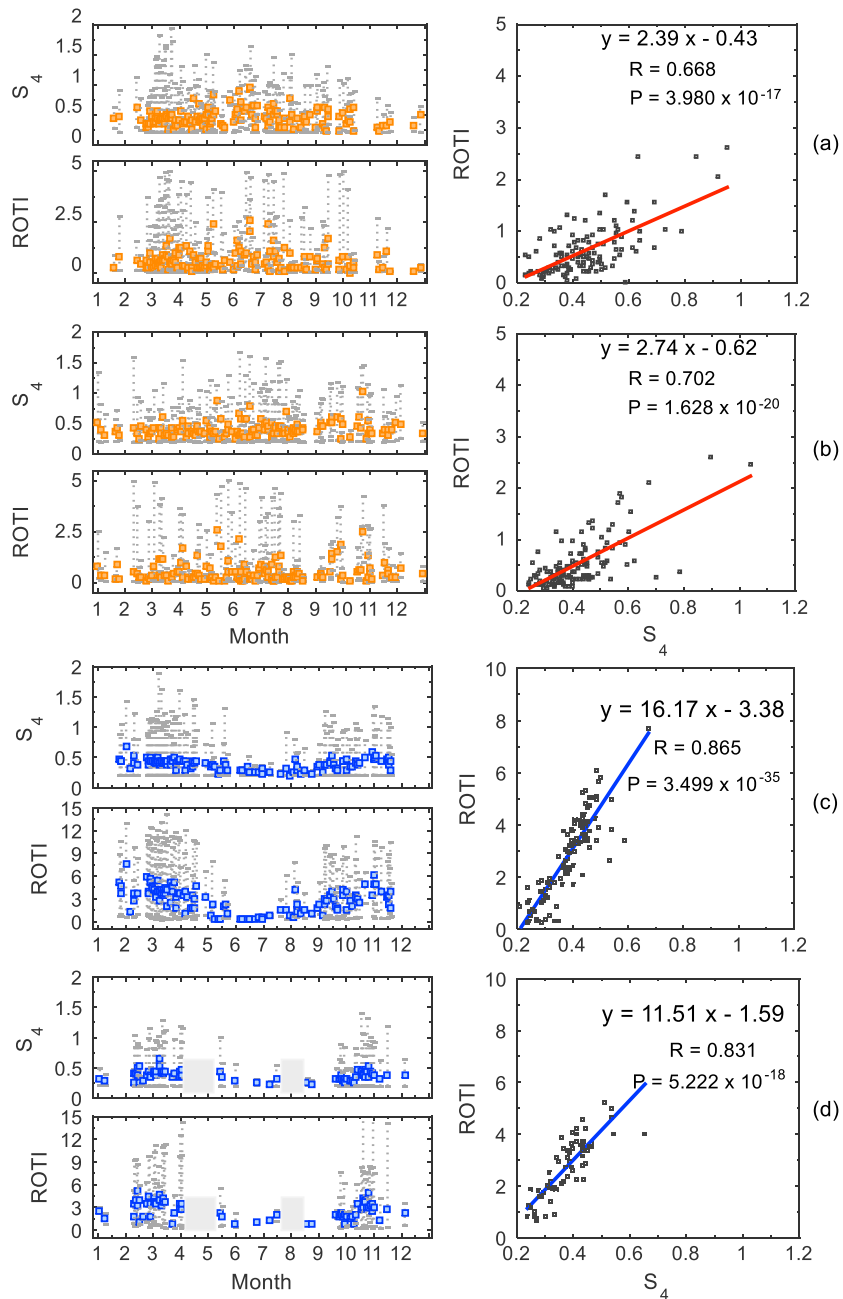


**Figure 5.** Nighttime (i.e., 18–06 LT)  $S_4$  and rate of change of total electron content index (ROTI) for the Constellation Observing System for Meteorology, Ionosphere, and Climate radio occultation and ground-based data are displayed as gray points in the left panels of (a) and (c) for 2014 and (b) and (d) for 2015, respectively. Their daily nighttime averages are shown in orange and blue points, respectively. Scatter plots of their daily averages are displayed with the correlation coefficient ( $R$ ) and significance level ( $P$ ) in the right panels. The ground-based data outages that occurred in April, May, July, and August of 2015 are marked as gray area.

ionospheric  $E$  and  $F$  regions and geographic locations. As seen in Figures 3 and 4, both  $E$  and  $F$  region irregularities were revealed in the RO observations, while the  $F$  region irregularities were mainly observed by the GB observations. In a general sense, the  $E$  region irregularities reached a maximum during the summer solstice (May–August) and a minimum during winter solstice (November–January). Their occurrences did not exhibit a solar dependence and a clear geographic distribution. The  $F$  region irregularities were prevalent during spring equinox (February–April) and autumn equinox (September–

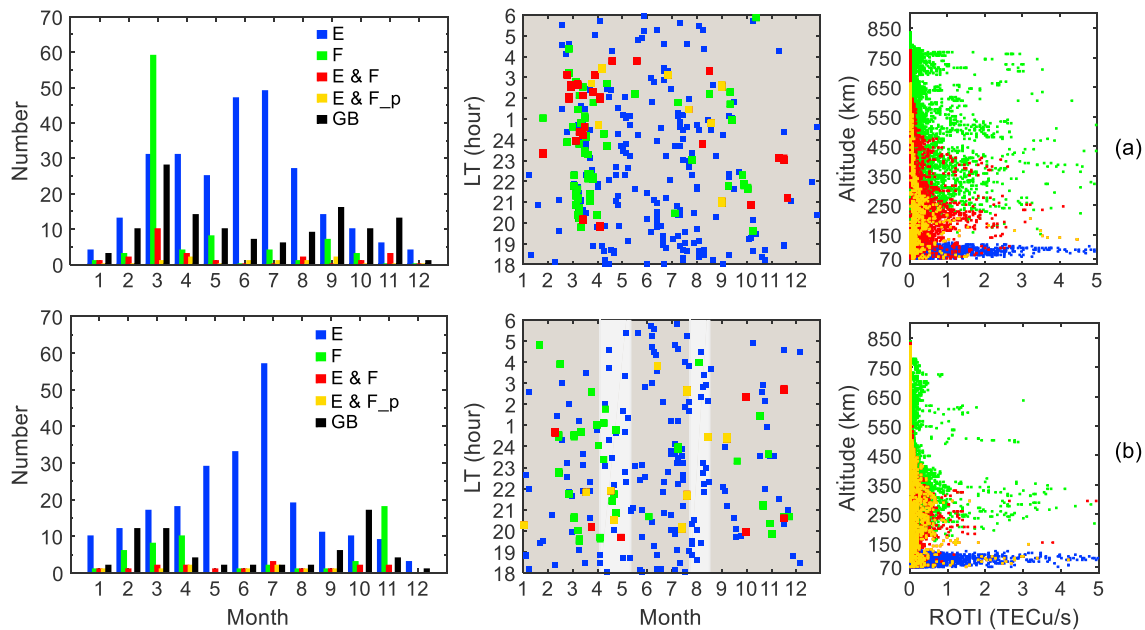


**Figure 6.** Occurrences of nighttime (i.e., 18–06 local time [LT]) *E* and *F* region irregularities for the years of (a) 2014 and (b) 2015. The blue and green colors that indicate the irregularities were observed at only *E* and *F* regions, respectively. The red color that represents both *E* and *F* region irregularities is observed by both radio occultation (RO) and ground-based (GB) RO data, while the yellow color represents the *E* and *F* region irregularities observed with RO data only. The black bar indicates the number of days with irregularities in GB observations. In the middle column, the GB data outages that occurred in April, May, July, and August of 2015 are marked as white area.

October) and were uplifted to higher altitudes in 2014. It may be noticed that there were data outages in spring and summer months of 2015. The geographic distributions of both RO and GB observations suggested that the *F* region irregularities were very pronounced in the south, especially in southwest China, as seen in Figures 3b and 4b. The higher occurrence in the south was attributed to the fact that the study area was located at the northern equatorial ionospheric anomaly region. By taking advantage of the RO and GB observations, we will give a detailed description of the occurrences of *E* and *F* region irregularities during nighttime and daytime in the following two sections.

### 3.2. Nighttime *E* and *F* Region Ionospheric Irregularities Associated With Scintillations

The nighttime variability (i.e., 18–06 LT) of ionospheric irregularities characterized by the ROTI and  $S_4$  values derived from both RO and GB data is displayed in Figure 5. As already shown in Figure 2, the ionospheric irregularities were revealed throughout 18–06 LT by RO observations but mainly during 20–03 LT by GB observations. It can be known from Figure 5 that the night-to-night variability of ionospheric irregularities manifests themselves by the varying values of ROTI and  $S_4$ . Associated with the nighttime scintillations, the ionospheric density irregularities observed by the RO ROTI increased in both the equinox and summer months, as shown in Figures 5a and 5b. In those months, the RO ROTI values increased to 2.5–5 TECu/s while they generally varied between 0 and 2.5 TECu/s in the winter months. Regarding the GB observations, as seen in Figures 5c and 5d, the increase of ionospheric density irregularities was only found in the equinox months. During the equinox months, the GB ROTI values reached above 6 TECu/min but was less than 3 TECu/min during the summer and winter months. It was worth noting in Figure 5 that the night-to-night variations in ROTI corresponded well to those of  $S_4$ . In the figure, the scatter plots of their daily averages demonstrated the correlations of their variations. As shown by small values of the significance level ( $P < 1 \times 10^{-10}$ ), a strong correlation was indicated between the ROTI and  $S_4$  variations. The correlation coefficients in 2014 and 2015 are 0.668 and 0.702 for the RO data sets, and they are 0.865 and 0.831 for the GB data sets, respectively. This suggests that the 1-s ROTI can represent the ionospheric density irregularities that cause scintillations of the GPS signal and may serve as an indicator of scintillations.

Figure 5 did not show whether the variability of ionospheric density irregularities occurred at *E* or *F* regions. Figures 3 and 4 suggested that both the *E* and *F* region irregularities were detected by the two data sets,

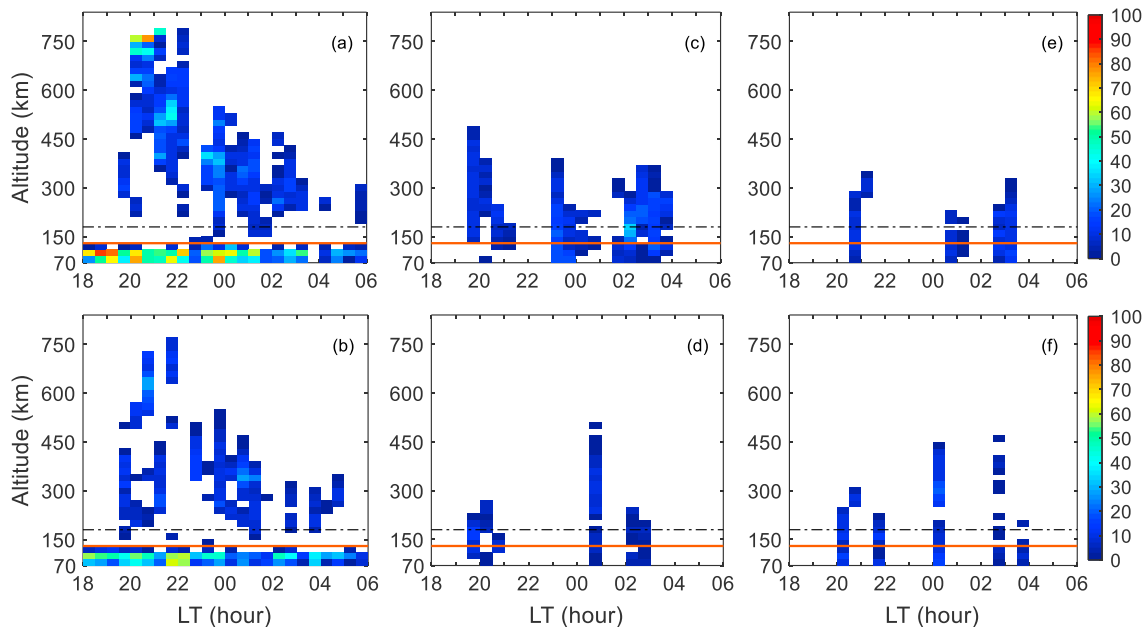


**Figure 7.** Altitude-local time (LT) variations in occurrences of nighttime (i.e., 18–06 LT) *E* and *F* region irregularities (a, b), simultaneous *E* and *F* region irregularities observed with (c, d), and without GB postsunset events (e, f) for 2014 (top row) and 2015 (bottom row). The red solid line represents the altitude at 130 km, while the dash-dotted line indicates the altitude at 180 km. The color bar represents the occurrence rate (%) of ionospheric irregularities during nighttime.

especially the RO observations. To describe the night-to-night variability of *E* and *F* region irregularities and the possibility of their linkage, Figure 6 presented the results revealed by the RO and GB observations. The occurrences of *E* and *F* region irregularities were examined based on the TP information of RO profile data. They are classified into four types: only *E* region, only *F* region, simultaneous *E* and *F* regions observed by both RO and GB data, and simultaneous *E* and *F* regions observed with RO data only. In Figure 6, the bar plot of their monthly occurrences, the LT-day variations in their occurrences, and the altitude-ROTI distributions of each type were displayed in the left, middle, and right columns, respectively.

From Figure 6, it is generally clear that all types of nighttime *F* region irregularities revealed by the RO observations occurred primarily during 20–03 LT and the type with *F* region irregularities only showed a distinct seasonal dependence. In March and April (September and October) of 2014, 63 (10) events were observed out of 90 RO events with *F* region irregularities only. In comparison, 18 (4) events were detected out of 51 RO events in 2015. Their occurrences were prevalent in the equinox months and seldom in the December winter solstice, coinciding well with the GB observations in 2014. The number of days with GB postsunset events was 28 (12) in March and 16 (6) in September of 2014 (2015). In Figure 6, the type with *E* region-only events was seen throughout the nighttime and with maximum (minimum) in the summer months (winter months). This prominent occurrence should contribute the increase of night-to-night RO ROTI and  $S_4$  values in the summer months as presented in Figure 5.

Regarding the simultaneous observations of *E* and *F* region irregularities during nighttime, two interesting features should be noticed in Figure 6. One is the striking occurrence of the type with GB postsunset events (red color) during the postmidnight hours (00–04 LT) and around the onset time (20 LT) of *F* region irregularities. The occurrences in the postsunset hours of 21–00 LT were insignificant. In 2014 (2015), out of 23 (7) RO events observed with this type, 18 (6) events were observed after midnight or near the onset time. In particular, the postmidnight occurrences (10) were salient in March 2014. Another is the observation of simultaneous *E* and *F* region irregularities by RO data only without GB events (yellow color). This type of events was rare (eight events in 2014 and seven events in 2015 if excluding those with data outages) and occurred throughout the postsunset hours of 20–04 LT.

In the *E* and *F* regions, the ionospheric density fluctuations are well demonstrated by the variation of the RO ROTI with altitudes, as shown in the right column of Figure 6. It is worth noting that the simultaneous *E* and *F* region irregularities were mainly observed below 450 km. To give a further analysis, the altitude-LT

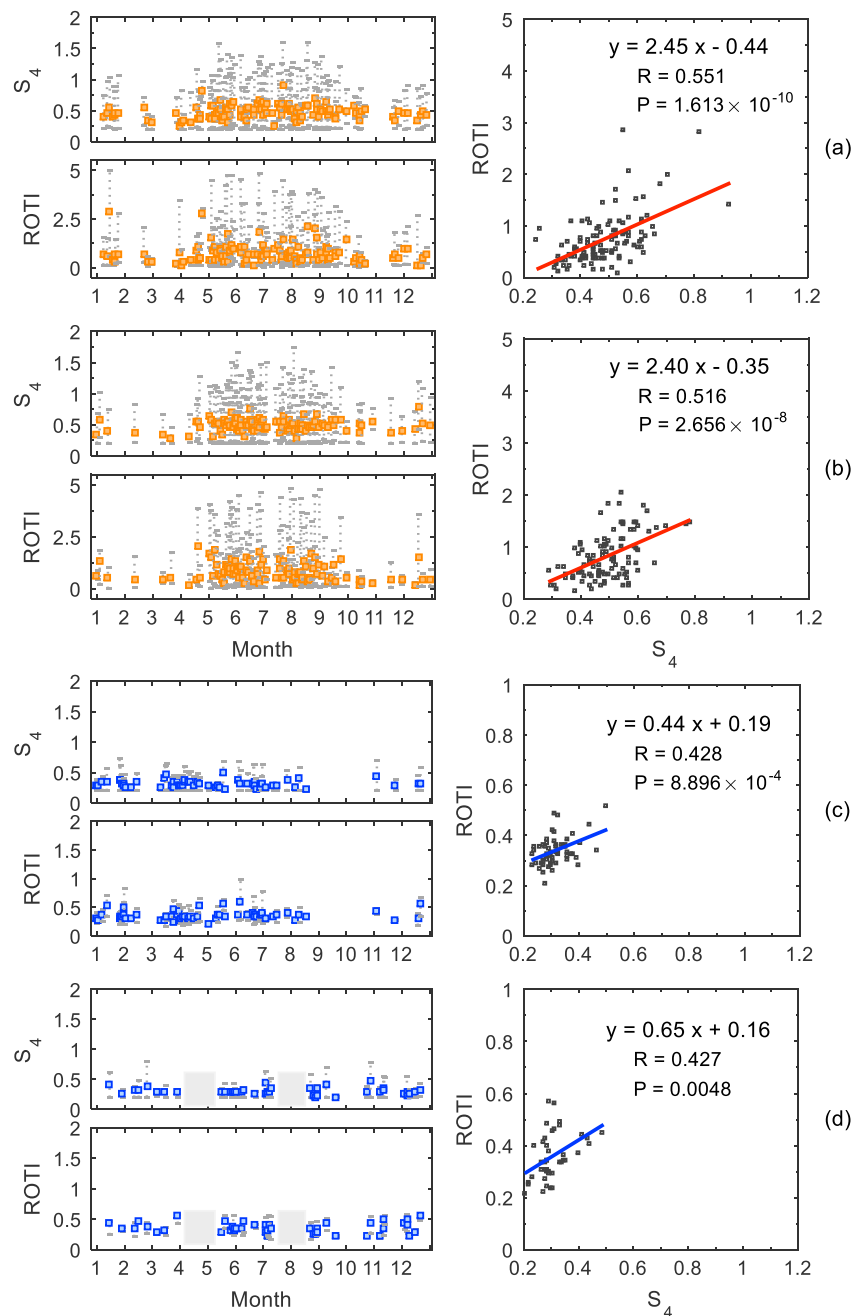


**Figure 8.** Same as Figure 5 but for daytime (i.e., 06–18 LT).

variations in occurrences of the *E* and *F* region irregularities are displayed in Figure 7. As can be seen from Figures 7a and 7b, the nighttime irregularities at the *E* region were dominant before the midnight period of 18–00 LT and mainly occurred at altitudes below 130 km; the occurrence of *F* region irregularities can be found at higher altitudes of around 800 km since the onset time (20–22 LT) and at the bottom of *F* region till 06 LT. The simultaneous *E* and *F* region irregularities, as illustrated in Figures 7c–7f, were observed predominantly around the onset time and after midnight. The ones with GB postsunset events appeared almost absent during 21–00 LT, which has been found in Figure 6. As also shown, their occurrences in the valley region (130–180 km) were more likely seen than those of only *E/F* region irregularities.

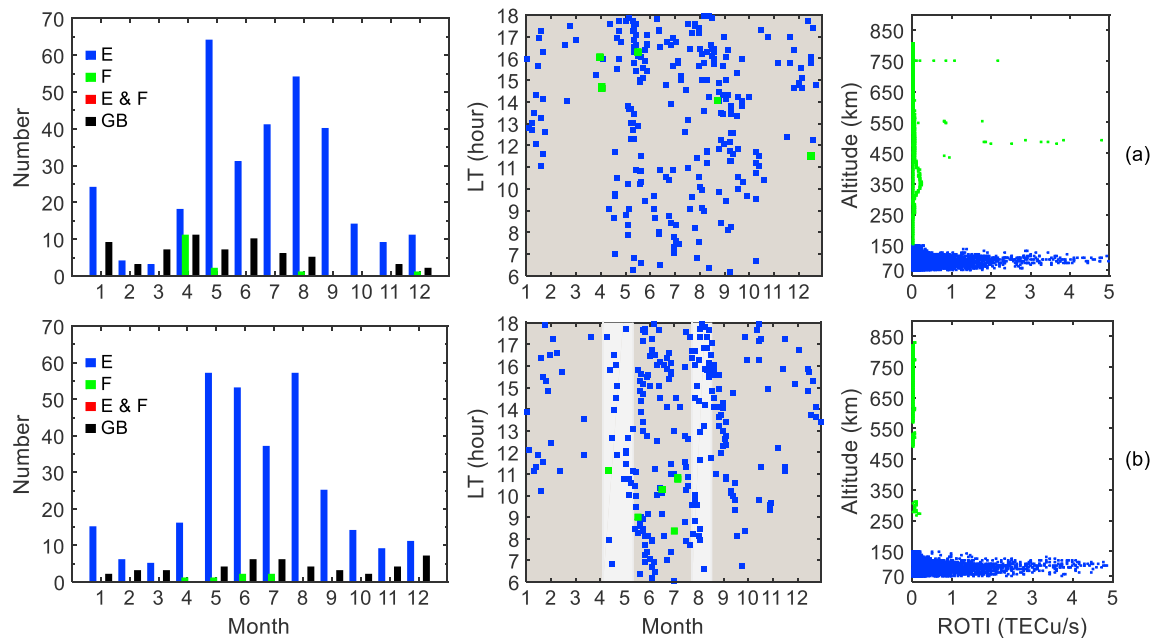


Figure 9. Same as Figure 6 but for daytime (i.e., 06–18 LT).

### 3.3. Daytime *E* and *F* Region Ionospheric Irregularities Associated With Scintillations

The daytime ionospheric irregularities were observed throughout the daytime period of 06–18 LT, as already seen in Figure 2. Figure 8 presented their day-to-day variability represented by the ROTI and  $S_4$  values over the study period. As shown in Figures 8a and 8b, a salient increase in the RO ROTI and  $S_4$  values was found in the summer months from May to August. The RO ROTI values in these summer months normally were above 2.5 TECu/s, while in other months they were generally less than 2.5 TECu/s. In comparison, as shown in Figures 8c and 8d, the day-to-day variability revealed by the GB observations was much more gentle. The GB ROTI values varied within a range of 0.2–1 TECu/min, and their seasonal dependence is not noticeable.

In Figure 8, a consistent variation in characterizing the daytime ionospheric irregularities between the ROTI and  $S_4$  values can be seen for both RO and GB observations. The scatter plots in Figure 8 showed their correlation levels. As observed, the correlation coefficients between their daily variations in 2014 and 2015 are 0.551 and 0.516 for the RO data sets, and they are 0.428 and 0.427 for the GB data sets, respectively. A high significance level ( $P < 1 \times 10^{-3}$ ) can be observed during daytime, but it is not as much as that during nighttime as given in Figure 5, especially for the GB observations. From Figures 5 and 8, it can be found that the variation of RO ROTI was consistent in characterizing ionospheric irregularities during both daytime and nighttime.

Figure 9 depicted the occurrences of the daytime ionospheric irregularities in the *E* and *F* regions. In the left column of Figure 9, it was evident from the RO observations that the daytime ionospheric irregularities were prominent in the *E* region and rarely observed in the *F* region. Also, no simultaneous *E* and *F* region irregularities were observed during daytime. In the middle column of Figure 9, it is found that the occurrence of *E* region irregularities was almost absent before the noontime period of 06–10 LT in the months from November to March. However, it was prevailing throughout the daytime in the summer months from May to August, which coincides with the notable increase of the RO ROTI values as shown in Figures 8a and 8b. In contrast, the occurrence of *F* region irregularities during daytime was rare and more likely in the spring and summer months. In both years 2014 and 2015, five RO events were observed with daytime *F* region irregularities. At different layers, as shown in the right column of Figure 9, the ionospheric density fluctuations are demonstrated by the altitude profiles of the RO ROTI values. It can be observed that the fluctuations in the *E* region are generally larger than those in the *F* region.

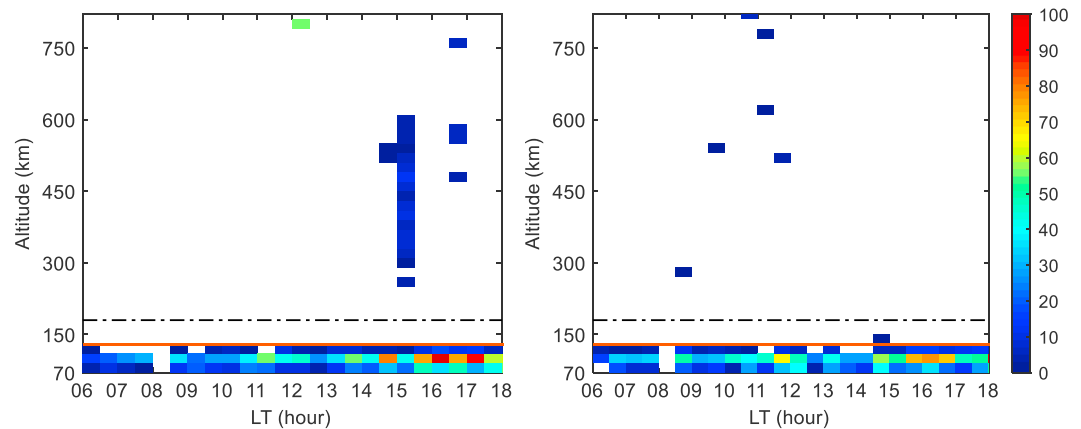


**Figure 10.** Altitude-local time (LT) variations in occurrences of daytime (i.e., 06–18 LT) *E* and *F* region irregularities for 2014 (left) and for 2015 (right). The red solid line represents the altitude at 130 km, while the dash-dotted line indicates the altitude at 180 km. The color bar represents the occurrence rate (%) of ionospheric irregularities during daytime.

Compared with the RO observations, the GB observations showed differences in characterizing the *E* region irregularities. As shown in Figure 9, in the summer months when the *E* region irregularities were dominant, a slight increase in the number of days with ionospheric irregularities was revealed by the GB observations. However, this was not obviously observed from the variations of the GB ROTI and  $S_4$  values presented in Figure 8. Likewise, during nighttime, this difference between the RO and GB observations was also observed, as seen in Figures 5 and 6.

The altitude-LT variations in occurrences of the daytime *E* and *F* region irregularities over the study period were illustrated in Figure 10. It showed that the occurrences of daytime *E* region irregularities are dominant during 15–18 LT and mainly occurred at altitudes of 90–110 km. The less occurrences before the noontime should be caused by their absence in the spring and winter months, as already shown in Figure 9. In the *F* region, the daytime irregularities were observed in the morning and late afternoon at the altitude range of about 300–840 km. The ionospheric irregularities in the valley region (130–180 km) almost disappeared during daytime.

## 4. Discussion

The *E* and *F* region irregularities (i.e., EPBs and Es) have been previously investigated using a variety of observations, such as radio scintillations, total electron content (TEC)-derived indices, in situ electron density, and airglow images (e.g., Burke et al., 2004; Kumar et al., 2016; Nishioka et al., 2008; Sun et al., 2016). The correspondence between the *F* region irregularities and scintillation occurrences was also statistically presented by simultaneously considering spread-*F* echoes in ionograms, GPS L1 band scintillation, and TEC-derived indices (e.g., Alfonsi et al., 2013; Shi et al., 2011). In the present study, their occurrences in the southeast China are illustrated by concurrently examining the GPS L1 band scintillations and TEC-derived indices retrieved from the COSMIC RO and GB GPS data. By examining the simultaneous observations of *E* and *F* region irregularities, a sign of the linkage of their nighttime occurrences is likely observed by the RO profile data.

### 4.1. Occurrences of Ionospheric *F* Region Irregularities

The temporal occurrence characteristics of nighttime *F* region irregularities by the COSMIC RO and GB data showed an overall consistency with the results from statistical studies that focused on the same Asian region using ionograms (Shi et al., 2011), GB GPS data (Kumar et al., 2016), and airglow images (Sun et al., 2016). Shi et al. (2011) has revealed that the strong range spread-*F* shows similarities in seasonal occurrence patterns with scintillations, which is also confirmed by Alfonsi et al. (2013) in the Southern American longitudinal sector. They suggested that the electron density depletions extending from the bottomside to the topside ionosphere are likely the cause explaining the correspondence. Our analysis showed a high correlation of ROTI with the GPS L band scintillations during nighttime, indicating that the ROTI well represents the electron density depletions accompanying scintillation occurrence.

Nishioka et al. (2008) used GB GPS data and suggested that the EPBs occurrences in the Asian sector correlate highly with solar activity and show asymmetry between two equinoxes (two solstices), which has also been presented in those abovementioned studies. By the RO and GB observations, the solar dependence could be clearly seen (Figures 1–4). Figures 5 and 6 suggested the asymmetry: occurrences in March equinox (June solstice) are higher than in September equinox (December solstice) of 2014. Recently, Sun et al. (2016) employed airglow images to conduct a statistical analysis of EPBs in China. Their data set in 2014 overlapped with our GPS data. In their observations, solstice asymmetry was not observed while our analysis did. A further comparison found that they precluded the effects of medium-scale traveling ionospheric disturbances (MSTIDs) during summer. As suggested by Alfonsi et al. (2013), the MSTIDs play an important roles in generating irregularities responsible for both spread-*F* and scintillation signatures. The MSTIDs effects on ionospheric density irregularities might be reflected by our GPS data set and showed the solstice asymmetry. Additionally, the differences between the two observation techniques might also be contributors. The maximum occurrences in the equinox months are normally explained by the theory of Tsunoda (1985). This theory, however, cannot explain the asymmetry. In the Asian sector, the meridional winds and background electron density are suggested to play a vital role in creating the equinoctial asymmetry, while the solstice asymmetry could result from the seasonal variations of *F* region field line-integrated conductivity (Nishioka et al., 2008; Sripathi et al., 2011, and references therein).

The geographic mappings of *F* region irregularities shown in Figures 3 and 4 appeared to reveal the tilted structures of EPBs. The EPB is tilted basically due to the vertical shear in the zonal plasma drift of the *F* region (Kelley et al., 2003). Based on the GB GPS data, Ji et al. (2015) has shown that the EPBs observed in the study region can be tilted either westward or eastward, and the tilt is generally less than 20° during the night. However, in Sun et al. (2016), their airglow images showed that most EPBs exhibited westward tilt with angles varying from 0° to 40°, and they suggested that the EPB depletions with larger westward tilt angles could be generated in a more westward region. Our results from the RO and GB observations confirmed this speculation as more scintillations are generated in the western region.

In spite of many researches on the statistical features of EPBs in the southeast China (Ji et al., 2015; Sun et al., 2016), they lacked description of altitudinal evolution. In our analysis, the *F* region irregularities can be detected at the altitudes up to ~800 km. The peak occurrences at high altitudes were found at 20–22 LT (Figure 7), showing an agreement with Burke et al. (2004) that compared longitudinal variability of the EPB occurrences at altitudes of ~840 and ~600 km. In general, the peak occurrences were seen during equinoxes of 2014 (Figures 3 and 4), due to the increased vertical drift of the *F* layer under solar active conditions (Abdu, 2001; Fejer et al., 1999).

The *F* region irregularities were also observed during daytime (Figure 9). In the past, very few studies have reported their dayside occurrences in the southeast China. Specifically, Kumar et al. (2016) used GB GPS data and suggested that the daytime EPBs were observed throughout 2001–2012 except during the high solar activity year 2002. From our analysis (Figures 8 and 9), it was suggested that their detection of EPBs might be influenced by the *E* region irregularities. Chen et al. (2017) presented two cases of dayside events observed in two geomagnetically quiet days by coherent scatter-phased array radar and suggested that the daytime irregularities may be the leftover of EPBs at previous nights. RO and GB observations showed that the daytime occurrences were seen at high altitude (above *F* region to ~800 km) and in the spring/summer months. There are four favorable conditions triggering daytime *F* region irregularities: at early morning, at low latitude, at high altitude, and during geomagnetic disturbance (Huang et al., 2013; Park et al., 2015, and references therein). The generation mechanism for geomagnetic disturbance days is attributed to the eastward electric field associated with disturbance dynamos. The one without ionospheric storm effects is still not fully understood as discussed in Park et al. (2015) and Chen et al. (2017). In our analysis, a detailed analysis of the dayside events revealed by the RO observations is beyond the scope of the present paper and it needs further investigations. The RO observations could be considered as one of potential data sources for the future study.

#### 4.2. Occurrences of Ionospheric *E* Region Irregularities

The *E* region irregularities (i.e., *Es*) were seldom studied in southeast China (e.g., Li, Ning, Patra, et al., 2011), especially in terms of their spatial-temporal occurrences. The spatial and temporal coverage of the COSMIC

RO observations revealed the temporal-spatial occurrence features of the *E* region irregularities, which cannot be obtained using GB instrumentation. Our analysis showed that the *E* region irregularities in southeast China occurred frequently in the afternoon and evening hours, in the summer months (May–August), and at altitudes of 90–110 km, while it occurred insignificantly in winter, showing a slight disagreement with those obtained from the global analysis of *Es* layers. Chu et al. (2014) presented the global morphology of *Es* layers retrieved from COSMIC RO observations. It showed that in the Northern Hemisphere the *Es* layers occurred predominantly during 06–00 LT in summer months (May to September) with the peak in July at the altitude range of 95–120 km. The *Es* occurrences with summer maximum have also been presented in other global analysis using the RO observations (Arras et al., 2008; Wu et al., 2005). Note that the retrieval methods of RO-measured *Es* layers differ among those work (Arras et al., 2008; Chu et al., 2014; Wu et al., 2005). This study exploits the 1-s RO GPS dual-frequency phase data as well as the scintillation data. Compared with the summer occurrences, an obvious difference in the diurnal occurrence time was observed in winter (Figures 6 and 9). This could be attributed to the control of tide waves with various periods (Chu et al., 2014). In winter, the temporal occurrence of *Es* layers is governed by the diurnal tides with shorter durations than that by the semidiurnal tides in summer, therefore leading to different diurnal occurrences.

By model simulations, Chu et al. (2014) showed that the formation of COSMIC-measured *Es* layers at low latitudes could not be well explained by the wind shear mechanism and suggested that the gravity waves (GWs) activity may play a significant role in their formation at low latitudes. This suggestion was supported by Hocke and Tsuda (2001) that showed that RO-measured *Es* layers were highly correlated with GWs activity over tropical convection zones of the Southern Hemisphere. In Hoffmann et al. (2013) that investigated the GWs activity and their source mechanisms on a global scale, it has been shown that the GWs activity is dominant in the months of May to August in Asia and the deep convection is considered as the major source mechanism. Regarding our study region, it is situated in the longitudes of intertropical convergence zone. Considering the *Es* layers with maximum occurrences in summer (May to August) for the region, it is asserted that their formation is likely affected by the combined effects of wind shear and GW activity. However, this needs to be further studied and validated. The GWs generated from the lower atmosphere can reach ionospheric heights and might enhance irregular neutral winds leading to the formation of *Es* irregularities (e.g., Parkinson & Dyson, 1998).

The RO-derived observations well revealed the occurrence features of ionospheric irregularities in this local region, as discussed above. By comparisons, the GB observations showed an agreement in the *F* region but a disagreement in the *E* region. For the *Es* layers, they typically had a horizontal extent of 10–1,000 km and a thickness of 0.5–5 km (Wu et al., 2005). The occulted GPS signals propagate through the ionospheric irregularities in horizontal paths so it can pass through a large portion of the field-aligned irregularities. In contrast, the GB static GPS receivers can continuously track GPS satellite signals in a view with high elevation angles but lack the horizontal observations. The GB GPS signals pass through the *Es* layers with paths shorter than the RO ones and therefore with limited ability to manifest *E* region irregularities in their observations.

### 4.3. Simultaneous Observations of *E* and *F* Region Irregularities

The simultaneous *E* and *F* region irregularities were observations from the RO profile data, and they were found only during nighttime. A few of them were observed without the GB postsunset irregularities. Their occurrences were found either before midnight or during postmidnight period and mainly at the bottomside of *F* region (Figures 6, 7e, and 7f). The COSMIC-retrieved irregularities were not revealed by the GB observations, suggesting that these irregularities may occur with scale sizes unable to be detected by GB observations. Meanwhile, it may also suggest that the evening perverse enhancement electric field responsible for the large uplift of the *F* layer should not be the primary factor seeding the R-T instability. Observed with the *E* region irregularities, several potential sources might play a role in the formation of *F* region irregularities, such as the *Es* instability (e.g., Tsunoda, 2007; Yizengaw et al., 2013) and the GWs activity generated by deep convection (Li, Ning, Abdu, et al., 2011). In association with those sources, the generated polarization electric fields and the GWs-induced ion density perturbation may provide favorable seeds for the growth of R-T instability.

It is worth noting the simultaneous observations of *E* and *F* region irregularities when the GB postsunset irregularities were detected. As shown in Figure 6, they were almost absent during postsunset hours of 21–00 LT.

They were predominant after midnight, especially in March 2014. It has been indicated by Sun et al. (2016) that the EPBs mainly occurred during 21–00 LT in equinoxes for 2014. The postmidnight *F* region irregularities at solar maximum are mostly the continuation of postsunset EPBs (Li, Ning, Abdu, et al., 2011). Thus, in the presence of postsunset irregularities, the postmidnight *F* region irregularities observed with the *E* region irregularities in the analysis may not be freshly generated but the continuation or fossil of postsunset EPBs. They were not generated due to the coupling of ionospheric *E* and *F* regions. However, it is interesting to find that they were almost absent during the occurrence period (i.e., 21–00 LT) of EPBs.

Previously, simultaneous observations of equatorial *E* and *F* region irregularities are made by various kinds of radars and ionosonde to investigate the coupling of ionospheric *E* and *F* regions. Abdu et al. (2003) used ionosonde observations and found that the *Es* layers disrupted in the presence of sunset *F* layer rise and that they reformed again after a break of  $\sim 3$  hr. Patra et al. (2004, 2005) employed radar observations and suggested that the disruption of *E* region irregularities was closely associated with the growth and development phase of EPBs. In the study region, Li, Ning, Patra, et al. (2011) utilized the VHF coherent scatter radar and revealed the weakening/disappearance of *E* region irregularities during the development of postsunset EPBs in equinoctial months. They all indicated that the *Es* layers could be weakened or disrupted with the coupling effects of the equatorial *F* region. Among them, different coupling processes were explained. In Abdu et al. (2003) the sheared vertical electric field associated with the postsunset EPBs was considered as the cause of *Es* disruption, while the polarization electric fields generated in association with the evening EPBs are suggested in those above other studies (Li, Ning, Patra, et al., 2011; Patra et al., 2004, 2005).

This study revealed the absence of simultaneous *E* and *F* region irregularities during the postsunset hours and their prominent presence after midnight. It could be related to the disruption/weakening of *E* region irregularities in the presence of EPBs and their reformation afterward. In other words, a sign of coupling of *E* and *F* regions during nighttime is likely revealed from the RO profile observations. As explained by Li, Ning, Patra, et al. (2011) and Patra et al. (2005), the polarization electric fields associated with the EPB bifurcations or the development phase of EPBs can be responsible for the disruption/weakening of *E* region irregularities. These electric fields can map to the low-latitude *E* region and inhibit their occurrences via the growth rate of gradient drift instability. They also showed that those electric fields could trigger the valley region irregularities (130–180 km). In our analysis, it was noticed that the irregularities in the valley region were mainly seen in the simultaneous observations of *E* and *F* region irregularities. As those kinds of irregularities are mainly detected by radars that can observe 3-m scale size of irregularities (e.g., Yokoyama et al., 2005), the RO-retrieved irregularities in this region may not be caused by the coupling processes. The RO profile observations were made with limb-viewing geometry, which may record irregularities at different altitudes.

## 5. Conclusions

We employed the COSMIC RO profile data and GB GPS observations to examine the occurrences of ionospheric *E* and *F* region irregularities/scintillations over a solar active period in the southeast China. By combining the GB GPS observation, this is the first time to utilize the RO profile data to concurrently investigate their temporal-spatial occurrences at a local scale and discuss the linkage between their daily occurrences. Through the analysis, the differences between the RO and GB GPS observations in characterizing ionospheric irregularities were revealed. The major findings from this locally integrated analysis are summarized as follows:

1. The *F* region irregularities exhibited maximum (minimum) activity during equinox (solstice) seasons and asymmetry between two equinoxes (solstices) at solar active year. Their temporal occurrences show a general agreement with the results of EPBs obtained based on airglow images and GB GPS data. Their 3-D geographic mapping revealed the westward tilted structure of EPBs and the altitudinal evolution of EPBs with time.
2. The *E* region irregularities with maximum (minimum) occurrences in summer (winter) were well presented by the RO observations, while GB observations did not show significant occurrences.
3. In the presence of postsunset *F* region irregularities, the simultaneous observations of *E* and *F* region irregularities appear absent before midnight, indicating that the coupling of *E* and *F* regions during night was possibly revealed by the RO profile data. This could be the first time observing a sign of coupling from space-based data set.

The radio scintillations and TEC-derived index (i.e., ROTI) retrieved from the RO profile data agreed well in characterizing ionospheric irregularities at a local scale. The combination of both data sources can complement the limitations of GB observations. In future work, several issues raised from this study need to be investigated, such as the daytime *F* region irregularities revealed by RO observations and the summer *E* region irregularities in association with GWs activity.

#### Acknowledgments

The present study was supported by the Hong Kong Research Grants Council (RGC) (project PolyU 5203/13E, B-Q37X) and the Hong Kong Polytechnic University (projects 4-BCBT and G-YBDA). The authors would like to thank the COSMIC Data Analysis and Archive Center (CDACC) for providing COSMIC data. The authors are very thankful for the suggestions by Alan Rodger and anonymous reviewers. The COSMIC data can be accessed via the CDACC website <http://cdaac-www.cosmic.ucar.edu/cdaac/>, and all the derived GPS data for the present study can be accessed at the link <https://doi.org/10.5281/zenodo.1213796>.

#### References

- Abdu, M. (2001). Outstanding problems in the equatorial ionosphere–thermosphere electrodynamics relevant to spread *F*. *Journal of Atmospheric and Solar-Terrestrial Physics*, 63(9), 869–884. [https://doi.org/10.1016/S1364-6826\(00\)00201-7](https://doi.org/10.1016/S1364-6826(00)00201-7)
- Abdu, M., MacDougall, J., Batista, I., Sobral, J., & Jayachandran, P. (2003). Equatorial evening prereversal electric field enhancement and sporadic *E* layer disruption: A manifestation of *E* and *F* region coupling. *Journal of Geophysical Research*, 108(A6), 1254. <https://doi.org/10.1029/2002JA009285>
- Alfonsi, L., Spogli, L., Pezzopane, M., Romano, V., Zuccheretti, E., De Franceschi, G., et al. (2013). Comparative analysis of spread-*F* signature and GPS scintillation occurrences at Tucumán, Argentina. *Journal of Geophysical Research: Space Physics*, 118, 4483–4502. <https://doi.org/10.1002/jgra.50378>
- Arras, C., Wickert, J., Beyerle, G., Heise, S., Schmidt, T., & Jacobi, C. (2008). A global climatology of ionospheric irregularities derived from GPS radio occultation. *Geophysical Research Letters*, 35, L14809. <https://doi.org/10.1029/2008GL034158>
- Basu, S., Basu, S., Huba, J., Krall, J., McDonald, S., Makela, J., et al. (2009). Day-to-day variability of the equatorial ionization anomaly and scintillations at dusk observed by GUVI and modeling by SAMI3. *Journal of Geophysical Research*, 114, A04302. <https://doi.org/10.1029/2008JA013899>
- Basu, S., Kudeki, E., Basu, S., Valladares, C., Weber, E., Zengingonul, H., et al. (1996). Scintillations, plasma drifts, and neutral winds in the equatorial ionosphere after sunset. *Journal of Geophysical Research*, 101(A12), 26,795–26,809. <https://doi.org/10.1029/96JA00760>
- Brahmanandam, P., Uma, G., Liu, J., Chu, Y., Latha Devi, N., & Kakinami, Y. (2012). Global S4 index variations observed using FORMOSAT-3/COSMIC GPS RO technique during a solar minimum year. *Journal of Geophysical Research*, 117, A09322. <https://doi.org/10.1029/2012JA017966>
- Burke, W., Gentile, L., Huang, C., Valladares, C., & Su, S. (2004). Longitudinal variability of equatorial plasma bubbles observed by DMSP and ROCSAT-1. *Journal of Geophysical Research*, 109, A12301. <https://doi.org/10.1029/2004JA010583>
- Carter, B., Yizengaw, E., Retterer, J., Francis, M., Terkildsen, M., Marshall, R., et al. (2014). An analysis of the quiet time day-to-day variability in the formation of postsunset equatorial plasma bubbles in the Southeast Asian region. *Journal of Geophysical Research: Space Physics*, 119, 3206–3223. <https://doi.org/10.1002/2013JA019570>
- Carter, B., Zhang, K., Norman, R., Kumar, V., & Kumar, S. (2013). On the occurrence of equatorial *F*-region irregularities during solar minimum using radio occultation measurements. *Journal of Geophysical Research: Space Physics*, 118, 892–904. <https://doi.org/10.1002/jgra.50089>
- Chen, G., Jin, H., Yan, J., Zhang, S., Li, G., Yokoyama, T., et al. (2017). Low-latitude daytime *F* region irregularities observed in two geomagnetically quiet days by the Hainan coherent scatter phased array radar (HCOPAR). *Journal of Geophysical Research: Space Physics*, 122, 2645–2654. <https://doi.org/10.1002/2016JA023628>
- Chu, Y.-H., Wang, C., Wu, K., Chen, K., Tzeng, K., Su, C.-L., et al. (2014). Morphology of sporadic *E* layer retrieved from COSMIC GPS radio occultation measurements: Wind shear theory examination. *Journal of Geophysical Research: Space Physics*, 119, 2117–2136. <https://doi.org/10.1002/2013JA019437>
- Fejer, B. G., & Kelley, M. (1980). Ionospheric irregularities. *Reviews of Geophysics*, 18(2), 401–454. <https://doi.org/10.1029/RG018i002p0401>
- Fejer, B. G., Scherliess, L., & De Paula, E. (1999). Effects of the vertical plasma drift velocity on the generation and evolution of equatorial spread *F*. *Journal of Geophysical Research*, 104(A9), 19,859–19,869. <https://doi.org/10.1029/1999JA900271>
- Hocke, K., & Tsuda, T. (2001). Gravity waves and ionospheric irregularities over tropical convection zones observed by GPS/MET radio occultation. *Geophysical Research Letters*, 28(14), 2815–2818. <https://doi.org/10.1029/2001GL013076>
- Hoffmann, L., Xue, X., & Alexander, M. (2013). A global view of stratospheric gravity wave hotspots located with Atmospheric Infrared Sounder observations. *Journal of Geophysical Research: Atmospheres*, 118, 416–434. <https://doi.org/10.1029/2012JD018658>
- Huang, C. S., La Beaujardiere, O., Roddy, P., Hunton, D., Ballenthin, J., & Hairston, M. (2013). Long-lasting daytime equatorial plasma bubbles observed by the C/NOPS satellite. *Journal of Geophysical Research: Space Physics*, 118, 2398–2408. <https://doi.org/10.1002/jgra.50252>
- Ji, S., Chen, W., Weng, D., & Wang, Z. (2015). Characteristics of equatorial plasma bubble zonal drift velocity and tilt based on Hong Kong GPS CORS network: From 2001 to 2012. *Journal of Geophysical Research: Space Physics*, 120, 7021–7029. <https://doi.org/10.1002/2015JA021493-T>
- Joshi, L., Patra, A., Pant, T., & Rao, S. (2013). On the nature of low-latitude  $E_s$  influencing the genesis of equatorial plasma bubble. *Journal of Geophysical Research: Space Physics*, 118, 524–532. <https://doi.org/10.1029/2012JA018122>
- Kelley, M. C., Makela, J. J., Paxton, L. J., Kamalabadi, F., Comberiate, J. M., & Kil, H. (2003). The first coordinated ground-and space-based optical observations of equatorial plasma bubbles. *Geophysical Research Letters*, 30(14), 1766. <https://doi.org/10.1029/2003GL017301>
- Kil, H., & Heelis, R. (1998). Global distribution of density irregularities in the equatorial ionosphere. *Journal of Geophysical Research*, 103(A1), 407–417. <https://doi.org/10.1029/97JA02698>
- Kintner, P. M., Ledvina, B. M., & de Paula, E. R. (2007). GPS and ionospheric scintillations. *Space Weather*, 5, S09003. <https://doi.org/10.1029/2006SW000260>
- Ko, C., & Yeh, H. (2010). COSMIC/FORMOSAT-3 observations of equatorial *F* region irregularities in the SAA longitude sector. *Journal of Geophysical Research*, 115, A11309. <https://doi.org/10.1029/2010JA015618>
- Kumar, S., Chen, W., Chen, M., Liu, Z., & Singh, R. P. (2017). Thunderstorm-lightning-induced ionospheric perturbation: An observation from equatorial and low-latitude stations around Hong Kong. *Journal of Geophysical Research: Space Physics*, 122, 9032–9044. <https://doi.org/10.1002/2017JA023914>
- Kumar, S., Chen, W., Liu, Z., & Ji, S. (2016). Effects of solar and geomagnetic activity on the occurrence of equatorial plasma bubbles over Hong Kong. *Journal of Geophysical Research: Space Physics*, 121, 9164–9178. <https://doi.org/10.1002/2016JA022873>
- Li, G., Ning, B., Abdu, M., Yue, X., Liu, L., Wan, W., & Hu, L. (2011). On the occurrence of postmidnight equatorial *F* region irregularities during the June solstice. *Journal of Geophysical Research*, 116, A04318. <https://doi.org/10.1029/2010JA016056>
- Li, G., Ning, B., Patra, A., Wan, W., & Hu, L. (2011). Investigation of low-latitude *E* and valley region irregularities: Their relationship to equatorial plasma bubble bifurcation. *Journal of Geophysical Research*, 116, A11319. <https://doi.org/10.1029/2011JA016895>

- Liu, J., Chen, S., Yeh, W., Tsai, H., & Rajesh, P. (2016). Worst-case GPS scintillations on the ground estimated from radio occultation observations of FORMOSAT-3/COSMIC during 2007–2014. *Surveys in Geophysics*, 37(4), 791–809. <https://doi.org/10.1007/s10712-015-9355-x>
- Mendillo, M., Meriwether, J., & Biondi, M. (2001). Testing the thermospheric neutral wind suppression mechanism for day-to-day variability of equatorial spread F. *Journal of Geophysical Research*, 106(A3), 3655–3663. <https://doi.org/10.1029/2000JA000148>
- Nishioka, M., Saito, A., & Tsugawa, T. (2008). Occurrence characteristics of plasma bubble derived from global ground-based GPS receiver networks. *Journal of Geophysical Research*, 113, A05301. <https://doi.org/10.1029/2007JA012605>
- Park, J., Stolle, C., Xiong, C., Lühr, H., Pfaff, R. F., Buchert, S., & Martinis, C. R. (2015). A dayside plasma depletion observed at midlatitudes during quiet geomagnetic conditions. *Geophysical Research Letters*, 42, 967–974. <https://doi.org/10.1002/2014GL026255>
- Parkinson, M., & Dyson, P. (1998). Measurements of mid-latitude E-region, sporadic-E, and TID-related drifts using HF Doppler-sorted interferometry. *Journal of Atmospheric and Solar-Terrestrial Physics*, 60(5), 509–522. [https://doi.org/10.1016/S1364-6826\(97\)00058-8](https://doi.org/10.1016/S1364-6826(97)00058-8)
- Patra, A., Sripathi, S., & Tiwari, D. (2004). Coupling effect of the equatorial F region irregularities on the low latitude E region instability processes. *Geophysical Research Letters*, 31, L17803. <https://doi.org/10.1029/2004GL020486>
- Patra, A., Yokoyama, T., Yamamoto, M., Saito, S., Maruyama, T., & Fukao, S. (2005). Disruption of E region echoes observed by the EAR during the development phase of equatorial spread F: A manifestation of electrostatic field coupling. *Geophysical Research Letters*, 32, L17104. <https://doi.org/10.1029/2005GL022868>
- Pi, X., Mannucci, A., Lindqwister, U., & Ho, C. (1997). Monitoring of global ionospheric irregularities using the worldwide GPS network. *Geophysical Research Letters*, 24(18), 2283–2286. <https://doi.org/10.1029/97GL02273>
- Schunk, R., & Nagy, A. (2009). *Ionospheres: Physics, plasma physics, and chemistry*. Cambridge, UK: Cambridge University Press.
- Shi, J., Wang, G., Reinisch, B., Shang, S., Wang, X., Zhrebotsov, G., & Potekhin, A. (2011). Relationship between strong range spread F and ionospheric scintillations observed in Hainan from 2003 to 2007. *Journal of Geophysical Research*, 116, A08306. <https://doi.org/10.1029/2011JA016806>
- Singh, S., Johnson, F., & Power, R. (1997). Gravity wave seeding of equatorial plasma bubbles. *Journal of Geophysical Research*, 102(A4), 7399–7410. <https://doi.org/10.1029/96JA03998>
- Sripathi, S., Kakad, B., & Bhattacharyya, A. (2011). Study of equinoctial asymmetry in the Equatorial Spread F (ESF) irregularities over Indian region using multi-instrument observations in the descending phase of solar cycle 23. *Journal of Geophysical Research*, 116, A11302. <https://doi.org/10.1029/2011JA016625>
- Sun, L., Xu, J., Wang, W., Yuan, W., Li, Q., & Jiang, C. (2016). A statistical analysis of equatorial plasma bubble structures based on an all-sky airglow imager network in China. *Journal of Geophysical Research: Space Physics*, 121, 11,495–11,517. <https://doi.org/10.1002/2016JA022950>
- Tsunoda, R. T. (1985). Control of the seasonal and longitudinal occurrence of equatorial scintillations by the longitudinal gradient in integrated E region Pedersen conductivity. *Journal of Geophysical Research*, 90(A1), 447–456. <https://doi.org/10.1029/JA090iA01p00447>
- Tsunoda, R. T. (2005). On the enigma of day-to-day variability in equatorial spread F. *Geophysical Research Letters*, 32, L08103. <https://doi.org/10.1029/2005GL022512>
- Tsunoda, R. T. (2006). Day-to-day variability in equatorial spread F: Is there some physics missing? *Geophysical Research Letters*, 33, L16106. <https://doi.org/10.1029/2006GL025956>
- Tsunoda, R. T. (2007). Seeding of equatorial plasma bubbles with electric fields from an E<sub>s</sub>-layer instability. *Journal of Geophysical Research*, 112, A06304. <https://doi.org/10.1029/2006JA012103>
- Tsunoda, R. T. (2010). On equatorial spread F: Establishing a seeding hypothesis. *Journal of Geophysical Research*, 115, A12303. <https://doi.org/10.1029/2010JA015564>
- Woodman, R. F., & La Hoz, C. (1976). Radar observations of F region equatorial irregularities. *Journal of Geophysical Research*, 81(31), 5447–5466. <https://doi.org/10.1029/JA081i031p05447>
- Wu, D. L., Ao, C. O., Hajj, G. A., de La Torre Juarez, M., & Mannucci, A. J. (2005). Sporadic E morphology from GPS-CHAMP radio occultation. *Journal of Geophysical Research*, 110, A01306. <https://doi.org/10.1029/2004JA010701>
- Yang, Z., & Liu, Z. (2016). Observational study of ionospheric irregularities and GPS scintillations associated with the 2012 tropical cyclone Tembin passing Hong Kong. *Journal of Geophysical Research: Space Physics*, 121, 4705–4717. <https://doi.org/10.1002/2016JA022398>
- Yeh, W. H., Liu, J. Y., Huang, C. Y., & Chen, S. P. (2014). Explanation of the sporadic-E layer formation by comparing FORMOSAT-3/COSMIC data with meteor and wind shear information. *Journal of Geophysical Research: Atmospheres*, 119, 4568–4579. <https://doi.org/10.1002/2013JD020798>
- Yizengaw, E., Retterer, J., Pacheco, E., Roddy, P., Groves, K., Caton, R., & Baki, P. (2013). Postmidnight bubbles and scintillations in the quiet-time June solstice. *Geophysical Research Letters*, 40, 5592–5597. <https://doi.org/10.1002/2013GL058307>
- Yokoyama, T., Patra, A., Fukao, S., & Yamamoto, M. (2005). Ionospheric irregularities in the low-latitude valley region observed with the Equatorial Atmosphere Radar. *Journal of Geophysical Research*, 110, A10207. <https://doi.org/10.1029/2005JA011208>